Flow Speed Sensor Based on Optical Microresonators

Elie R. Salameh*
Southern Methodist University, Dallas, Texas 75205
Alexandra K. Wise†
University of Colorado Boulder, Boulder, Colorado 80309
Jaime da Silva* and M. Volkan Ötügen‡
Southern Methodist University, Dallas, Texas 75205
and
Dominique Fourguette§
Michigan Aerospace Corporation, Ann Arbor, Michigan 48108

A compact flow velocity sensor based on dielectric optical microresonators is demonstrated. In this novel LiDAR-based sensor concept, velocity Doppler shifts from Mie-scattered light are determined using whispering gallery mode (WGM) optical resonators. The microresonators could replace Fabry–Perot interferometers and other optical frequency discriminators often employed in remote sensing applications, thereby significantly reducing the size and weight of the measurement system, making it suitable for flow diagnostics for both earthbound and airborne platforms. Two sets of experiments are carried out to assess the feasibility of the sensor concept. In the first-level proof-of-concept experiments, the tangential velocity of a solid rotating disk is measured using a sphere microresonator, with encouraging results. In follow-up experiments, velocity measurements near the exit of an air jet nozzle are carried out. The air is seeded with water droplets, and the Mie-scattered light is analyzed using on-chip ring resonators. Both single-point and jet profile measurements are made. The results demonstrate the feasibility of a WGM microresonator-based flow sensor.

Nomenclature

c	=	speed of light, m/s
D	=	diameter of nozzle at exit, mm
dA	=	differential overlap area, m^2
E_1	=	electric field distribution of coupling side 1, V/m
E_2	=	electric field distribution of coupling side 2, V/m
E_2^*	=	complex conjugate of E_2, V/m
$\boldsymbol{k_0}$	=	wave vector of incident light, rad/m
$\boldsymbol{k_S}$	=	wave vector of collected light, rad/m
m	=	circumferential integer mode number
n	=	refractive index
Q	=	resonator optical quality factor
R	=	radius of resonator, m
r	=	radial distance from the jet centerline, mm
V	=	velocity vector, m/s
V_a	=	projection of velocity vector along $(\boldsymbol{k_S} - \boldsymbol{k_0})$ direction, m/s
x	=	streamwise distance from nozzle exit plane, mm
α	=	angle between $\boldsymbol{k_0}$ and $\boldsymbol{k_S}$, rad
Δf	=	Doppler frequency shift, Hz
$\Delta \lambda$	=	wavelength shift, m
$\delta \lambda$	=	resonator linewidth in the wavelength spectrum, m
η	=	coupling efficiency from mode overlap integral
θ	=	angle between $\boldsymbol{k_0}$ and V, rad
κ	=	angular product factor
λ	=	operating wavelength, m
λ_R	=	relative wavelength, pm
ρ	=	concentric misalignment between fiber and telescope focus, μm
Ω_R	=	disk rotational speed in revolutions per second, Hz

*Research Assistant, Mechanical Engineering Department.
†Research Assistant, Ann & H.J. Smead Department of Aerospace Engineering Sciences.
‡Senior Associate Dean and Professor of Mechanical Engineering. Associate Fellow AIAA.
§Vice President of R&D, Visiting Research Professor of Mechanical Engineering, Southern Methodist University, Dallas; currently Senior Remote Sensing Engineer at Perikin Enterprises, Albuquerque, NM 87102. Associate Fellow AIAA.

I. Introduction

AIR- and space-borne optical measurements have gained increased importance over the last few years due to the interest in characterizing atmospheric quantities, such as the temperature profile [1,2], chemical species and contaminant concentration [3–6], and cloud formation and weather forecasting [7–11]. In addition to applications in Earth science, atmospheric characterization is of interest for interplanetary missions, especially for Mars. Air data sensing is of strong interest, and has been accomplished by stationary and mobile instrumentation using terrestrial (fixed research station and motor vehicle based), airborne (drones, weather balloons, airplanes), as well as low-Earth orbit (both CubeSats and traditional satellite missions) platforms [12–15]. Another type of atmospheric measurement relates to the entry, descent, and landing of spacecraft, entry demonstrator modules, and sounding rockets [16–19]. In these applications, the parameter of interest is the speed of the craft moving through a stagnant atmosphere.

Existing earthbound and airborne systems employing nonintrusive optical methods for wind measurements consist of a variety of techniques, such as laser Doppler velocimetry [20–23], particle image velocimetry [24,25], and laser imaging detection and ranging (LiDAR) systems using coherent Doppler measurements [26–28]. Airborne sensing in the absence of aerosols is typically performed using LiDAR systems with direct detection capabilities [29], which can offer robust and highly sensitive measurements, as well as high signal-to-noise ratios. However, their sensing elements (analyzing the backscattered light for Doppler shift) often employ Fabry–Perot interferometers operating in imaging mode along with two-dimensional cameras [30,31], or other, similarly complex and bulky, optical systems. These signal analysis modules are generally

more susceptible to external disturbances (especially vibration). This paper proposes an alternate approach for the analysis of the scattered light in which a whispering gallery mode (WGM) optical microresonator, along with a photodetector (photodiode or photomultiplier tube), is used to determine the Doppler shift. The approach significantly reduces the size and weight of the detection subcomponent of remote sensing systems, particularly in the case of Fabry–Perot-based instruments. As shown in Fig. 1, the Fabry–Perot interferometer and the two-dimensional array detector are replaced by a WGM microresonator and a photodetector.

In the present study, two sets of experiments are designed and performed. As a first step, the concept is tested by measuring the tangential velocity of a solid rotating disk. Several signal processing options are considered in these experiments. With the experience gained from these results, a second set of experiments is performed, this time near the exit plane of a water spray nozzle.

II.   Measurement Principle

In typical direct detection Doppler LiDAR systems (Fig. 1, left), the backscattered light from particulates or gas molecules is captured and directed (either by using a set of collecting optics or via an optical fiber) to a Fabry–Perot interferometer. At the output of the interferometer, the interference pattern is captured by a charge-coupled-device camera, and the movement of the pattern due to the Doppler shift in the collected light is analyzed to determine the gas velocity. In this configuration, the wavelength of the laser is fixed and the Fabry–Perot interferometer is used in the imaging mode. In the proposed configuration (Fig. 1, right), a scanning laser is used, and the scattered light is coupled into a single-mode optical fiber or a waveguide, and directed to a WGM resonator. The WGM resonator is a circular dielectric cavity (in the present study we use both sphere- and ring-shaped resonators). The collected light is tangentially introduced into the resonator via evanescent coupling from a single-mode optical fiber or an on-chip waveguide, as shown in Fig. 2. The optical fiber/waveguide serves as an input/output conduit. When the input light is tuned across a narrow wavelength range (by scanning the laser), optical resonances are observed as sharp dips at the output of the fiber/waveguide, as depicted in the figure. For a resonator of radius R and refractive index n, the approximate resonance condition is given by

$$2\pi R n = m\lambda \tag{1}$$

This measurement technique is similar to that of frequency-modulated continuous wave interference systems [32]. In this case, the WGM resonators act as temporally ultrastable wavelength discriminators, and Doppler shifts are directly determined from shifts in the transmission spectrum (see Fig. 2). The main advantage of this approach is the measurement of the Doppler shift as direct time-domain delay instead of relying on the frequency and phase measurements obtained from optical heterodyning. WGM resonators also typically possess extremely high optical quality factors Q, where $Q = \lambda/\delta\lambda$. High Q-factors are associated with low optical losses and
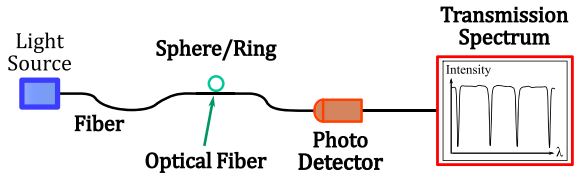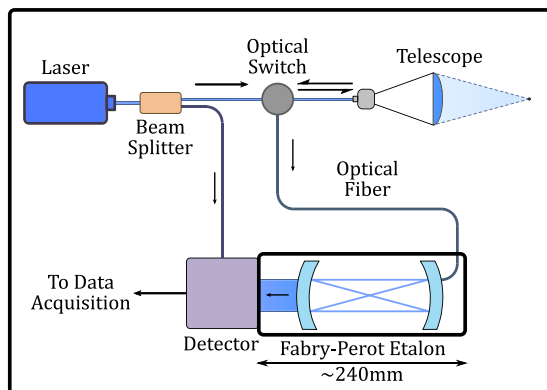
narrow resonance linewidths. For certain microresonator geometries, Q values can be as high as 10^7 or 10^8 [33]. Large Q values allow for extremely high resolution in the measurement of wavelength shifts (due to exceedingly small resonance linewidths), which has led to the development of several WGM-resonator-based sensor concepts in recent years. These sensor concepts include force [34], pressure [35], wall pressure [36], wall shear stress [37], electric field [38], as well as magnetic field sensors [39]. In the present application, a small change in the wavelength of the scattered light shifts the location of the dips in the transmission spectrum shown in Fig. 2, allowing for the detection of Doppler shifts caused by changes in the particle velocities.

As described in Fig. 3, when the incident laser wave vector k_0, collecting wave vector k_S, and velocity vector are all on the same plane, the relationship between the WGM frequency shift and the velocity of the gas is given by [40]:

$$\Delta f = \frac{2V_a}{\lambda} \sin\left(\frac{\alpha}{2}\right) \tag{2}$$

The projection V_a of the velocity vector along the direction $k_S - k_0$ is

$$V_a = \boldsymbol{V} \cdot (\boldsymbol{k_S} - \boldsymbol{k_0}) \tag{3}$$

Therefore, the velocity magnitude can be expressed in terms of Doppler wavelength shift as

$$V = -\frac{c \cdot \Delta\lambda}{2\lambda} \frac{1}{[\cos\theta(\cos\alpha - 1) + \sin\theta\sin\alpha]\sin\left(\frac{\alpha}{2}\right)} \tag{4}$$

Fig. 2   Schematic representation of the WGM resonator and its operation.
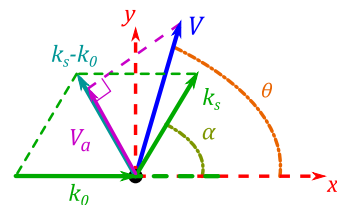
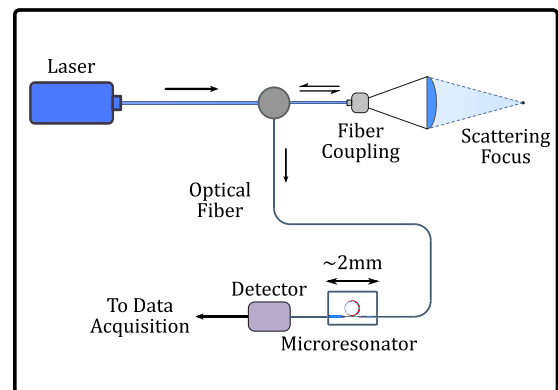**Fig. 3   Doppler angles and measured velocity on a plane.**

Fig. 1   Left: generalized Fabry–Perot-based LiDAR; right: proposed WGM resonator-based system.

Setting $\kappa = [\cos\theta(\cos\alpha - 1) + \sin\theta\sin\alpha]\sin(\alpha/2)$, Eq. (4) becomes

$$V = -\frac{c \cdot \Delta\lambda}{2\lambda\kappa} \qquad (5)$$

where $\kappa \in [-2, 2]$.

III. Rotating Disk Experiment

A. Experimental Setup

A schematic of the experimental setup is shown in Fig. 4. The output of the 9 mW, 639 nm Littman–Metcalf cavity diode laser is focused on the edge of the rotating disk [41]. The scattered light from the edge of the disk is collected, collimated, and subsequently reduced in diameter to facilitate the coupling into a single-mode optical fiber. The mode-field diameter of the fiber core is ~3.6 μm. The fiber-coupled light is then directed through a tapered section of the fiber, where it is coupled into a ~500 μm-diameter spherical silica resonator. The transmitted light is collected by a photodiode, and its output is discretized by a 12-bit analog-to-digital converter. The data is analyzed on a desktop computer. A magnetic tachometer is used to determine the rotational speed of the disk. Approximately 1.6 mW of light scattered from the disk's edge is captured by the collecting optics, and about 13.5 μW is coupled into the optical fiber. The light power captured by the photodetector after the tapered fiber region is approximately 0.05 μW. This corresponds to a total light loss of ~99.63% between the collecting fiber coupler and the photodetector, which is poor, but not unexpected, given the significant insertion and scattering losses in the fiber coupling and tapering sections, respectively. Additional losses from setup misalignment are also significant due to the highly specular surface of the rotating disk. Thus, optical coupling and transmission efficiency pose a challenge in the current setup. When an optical fiber is used for coupling light into the resonator, the fiber must be tapered down to a diameter of ~10 μm to sufficiently expose the evanescent field, resulting in significant additional light loss through scattering in the tapered region. This loss can be mitigated by using the integrated waveguide–ring resonator system, such as that presented in the next set of experiments. The integrated resonator–waveguide system does not require tapering for efficient light coupling between the waveguide and the resonator. Thus, the only significant coupling loss occurs at the input and output ends of the waveguide. For a more comprehensive description of the experimental setup and procedure, the reader is referred to [42].

B. Results

The laser wavelength is scanned at a rate of 700 Hz by a ramp-waveform driver signal from a function generator. The disk frequency Ω_R is varied between 48 and 240 rotations per second, corresponding
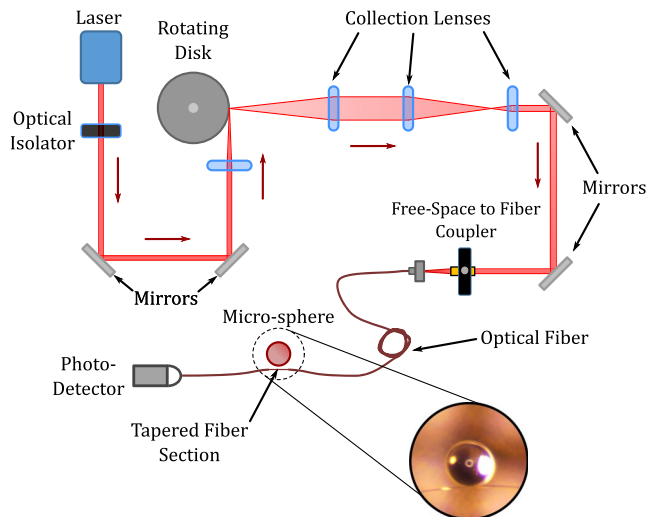
to edge tangential velocities of 14.3 m/s and 71.6 m/s, respectively. The collected signal (transmission spectrum) is digitized at 6000 data points per wavelength scan, phase-locked, and ensemble-averaged over approximately 600 successive laser scans for each disk speed. Figure 5 shows the transmission spectra in the vicinity of a selected WGM resonance dip for a single laser scan. The corresponding ramp signal (driver voltage) is also shown for reference. As the disk's rotational frequency increases, the resonances move to the right (longer wavelengths) due to the Doppler shift.

The Doppler shifts vs disk rotational speed are shown in Fig. 6. Data processing consists of phase-locked averaging of 600 individual laser scans to obtain an ensemble-averaged transmission spectrum at a given disk rotational speed. Two sets of experiments are performed with two different setups, at two different times. The measured Doppler shifts are determined by applying cross correlation between each ensemble-averaged scan and a reference scan. The reference scans used correspond to disk rotational frequencies of 48 Hz for experiment 1 and 60 Hz for experiment 2. The optics are set up such that $\alpha = -90$ deg and $\theta = -180$ deg (referring to Fig. 3). The solid line represents the WGM shifts calculated using Eq. (4). The dotted lines represent the systematic uncertainty of the measured Doppler shift due to misalignment in α and θ. WGM shifts for two sets of angle misalignments, ± 3 deg and ± 5 deg, are shown in the figure. Even a relatively modest angle misalignment affects the measured Doppler shifts considerably, resulting in the slightly different slopes obtained in the two sets of measurements.

Several factors influence the signal quality in the preceding experiments. Imperfections in the disk concentricity and edge flatness cause
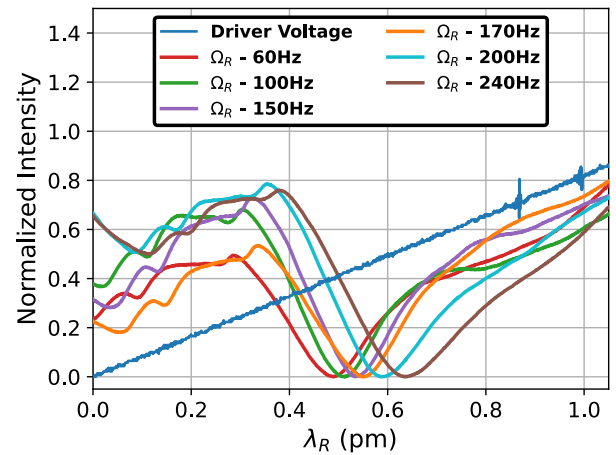
Fig. 5 Transmission spectra around the selected resonance for several Ω_R.

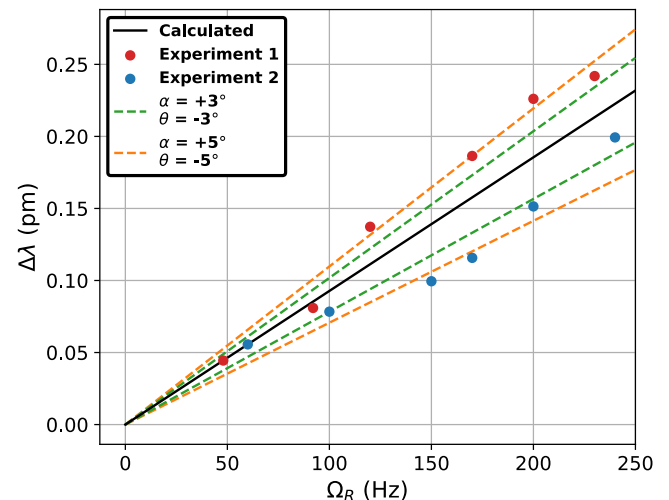**Fig. 4 Setup for the rotating disk experiment.**

Fig. 6 WGM shift for various disk rotational speeds.

the edge of the disk to "wobble," leading to considerable degradation and loss of signal on the collection side, resulting in poor signal-to-noise ratios. This is further amplified due to the freestanding nature of the optics, and the high precision required in free-space-to-fiber coupling. As explained in Sec. IV, use of integrated optics significantly improves alignment stability and signal quality. Despite these factors, the experiments demonstrate the feasibility of the measurement technique.

IV. Jet Velocity Measurements

A. Experimental Setup

An improved opto-electronic arrangement is set up and measurements are made at the exit of an internal-mixing water-atomizing spray nozzle. Mie scattered light is collected and analyzed to determine Doppler shifts. The nozzle exit is circular, with a diameter of $D = 1.27$ mm. The nominal droplet diameter is ~25 μm.

For these experiments, pigtailed on-chip microring resonators and integrated waveguides are used instead of the sphere resonators and tapered optical fibers employed previously. A schematic of the experimental setup is shown in Fig. 7.

Referring to Fig. 3 and Eq. (5), larger $|\kappa|$ values yield higher resolutions in measured velocity. Figure 8 shows the variation of $|\kappa|$ with α and θ. The experiment is set up to measure the streamwise velocity, with the incident and collection optics directions both at 45° to the jet axis. This results in laser beam and light collection angles of $\alpha = 90$ deg and $\theta = 135$ deg, resulting in $|\kappa| = 1$, as highlighted in Fig. 8.
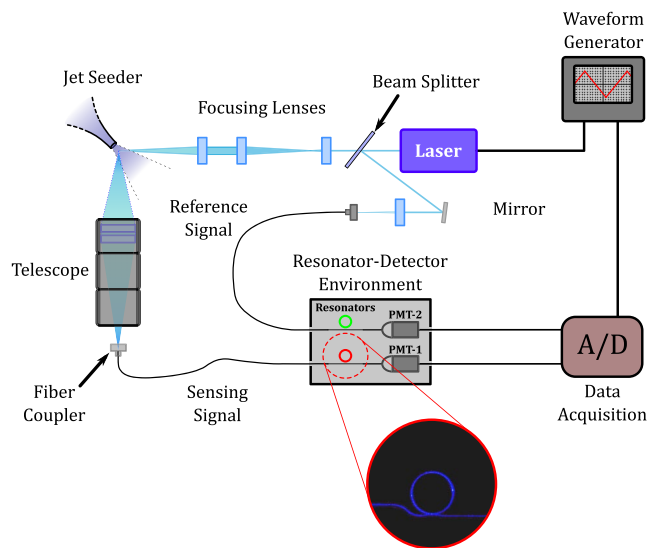

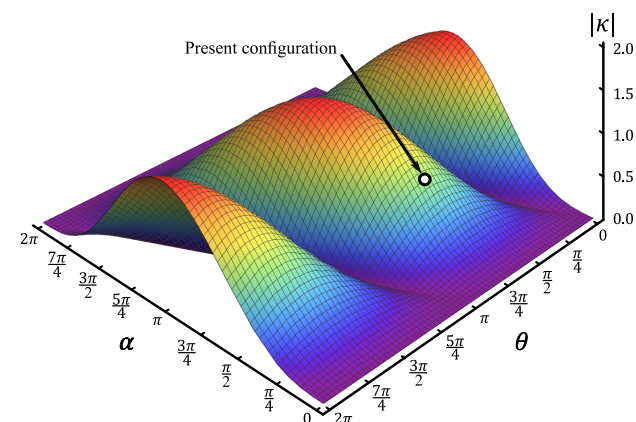**Fig. 7   Experimental setup for the jet velocity measurements.**

Fig. 8   Variation of $|\kappa|$ with α and θ. The circle indicates the configuration used in the present experiment.

A solid-state continuous-wave tunable laser is used for this experiment, with a nominal power and a wavelength of 120 mW and 461 nm, respectively. The laser wavelength is scanned by varying the voltage on the piezo-mechanical element that acts on the laser resonator cavity grating. The mode-hop-free frequency scanning range of the laser is ~20 GHz. The probe waist, with a diameter of ~4 μm, is formed using a set of focusing lenses, as shown in Fig. 7. A benchtop telescope is used as the collection optic. At the output of the telescope, a free-space-to-fiber adapter feeds collected light into a single-mode optical fiber. At the other end, the fiber is pigtailed into a microchip that contains an embedded waveguide and ring resonator. On the opposite end of the chip, light from the waveguide terminates at a photomultiplier tube (PMT) (Fig. 7). Light coupling from the telescope into the single-mode fiber is of chief concern, as the largest signal loss is incurred in this step. The coupling efficiency η between the telescope and the fiber can be calculated from the overlap integral [43]:

$$\eta = \frac{|\int E_1 E_2^* \, \mathrm{d}A|^2}{\int |E_1|^2 \, \mathrm{d}A \int |E_2|^2 \, \mathrm{d}A} \quad (6)$$

Subscripts 1 and 2 refer to the telescope and fiber sides, respectively. An estimate of the electric field distribution for the optical fiber used is calculated using finite-element analysis, and is displayed in Fig. 9. The solid line in the figure represents the fiber core with a diameter of 3 μm. The field distribution of the free-space light coming from the telescope and focused on the fiber face is assumed to be Gaussian with a diameter of 4 μm. The coupling efficiency values are calculated using Eq. (6) for a range of concentric misalignment values ρ. The dependence of η on ρ is plotted in Fig. 10. The maximum possible coupling efficiency is ~93.57% when $\rho = 0$.

The figure also demonstrates that even a small misalignment results in a significant reduction in coupling efficiency. This highlights the difficulty in using freestanding optical components for this type of coupling (as is the case with the presented preliminary experiments), as opposed to using a fully integrated optical system, such as Bragg gratings, for coupling.

Ring resonator–waveguide chips are fabricated using the silicon-nitride-on-insulator method, which affords robust waveguide–resonator coupling. The diameter of the resonators is ~800 μm. The on-chip design also results in well-defined and isolated WGM dips. The free-spectral range of the resonators is ~65 GHz. In this configuration, the resonator supports only one WGM mode, unlike the sphere resonator–fiber arrangement, where multiples of spatial (in the spherical resonator) and transverse (in the fiber waveguide) modes can exist within the tuning range (see Fig. 5).
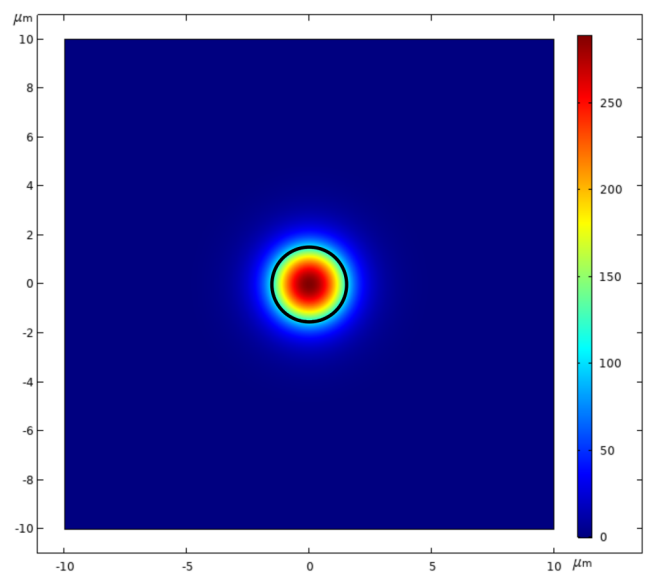

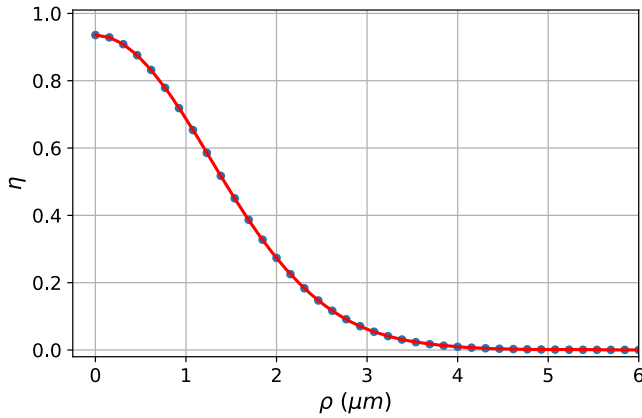**Fig. 9   Electric field distribution for optical fiber core (V/m).**

Fig. 10   Coupling efficiency vs concentric misalignment between fiber core and telescope focus.

Due to thermal instability, the laser wavelength drifts over time. As shown in Fig. 7, a second resonator is used to account for the wavelength drift of the laser. This reference microresonator is also pigtailed and is used along with the sensing resonator to remove the effect of laser wavelength drift from the data. Approximately 10% of the light from the laser is directed through a 90:10 beam splitter into a series of mirrors and lenses that focus onto a single-mode optical fiber. This is then coupled into the pigtailed reference resonator and terminated at another PMT. Both resonators are enclosed in the same environment to minimize external effects. The PMT outputs are digitized by a 12-bit analog-to-digital converter, and processed on a personal computer to determine the WGM shifts.

The resonators must be calibrated against a reference. This is necessary because the scanning range of the laser is smaller than the free-spectral range of the resonator, as discussed in the next section. A Fabry–Perot interferometer (FPI) with a narrow free-spectral range (~1.5 GHz) is used as the reference. Part of the laser output is directed into the FPI, and the rest is coupled into each of the two resonators, one at a time. The calibration results are shown in Fig. 11.

The Q-factors are calculated for each resonator from the transmission spectra at $\lambda = 461$ nm. The Q-factors for the sensing and reference resonators are determined to be ~4×10^5 and ~2×10^5, respectively. These factors are modest due to the small resonator diameters (~800 μm). Employing larger resonators would increase these factors significantly. On-chip ring resonators with diameters of 25 mm are reported to have Q-factors as high as 10^7 [33].

The laser is tuned by changing the voltage into the piezo-actuator that controls its cavity length. This input voltage is a double-sided ramp (triangular) signal with a DC bias. The ramp component of the signal tunes the laser to reveal the transmission spectrum of the resonators, while the bias voltage on the ramp changes the location of the resonances in the transmission spectrum, mimicking the Doppler shift. The resonator shifts in the graphs (y axis) are shown

in terms of the bias voltage into the laser, whereas the actual wavelength shifts (x axis) are determined from the FPI. The error bars along x axis represent the uncertainty related to the minimum measurable wavelength shift from the FPI. Using a conservative approach, it is taken to be the half-width at half-max of the FPI resonance peak (estimated to be ~5.9 fm). The error bars along y axis are the root-mean-square deviations between the measured WGM shifts and the linear fit. They are calculated to be ~6.7 mV for the sensing resonator, and ~5.3 mV for the reference resonator.

B.   Results

As indicated in Fig. 7, a triangular waveform from a function generator drives the laser frequency, corresponding to a scanning range of ± 20 GHz. This is within mode-hop-free tuning range of the laser. Although it is sufficiently wide to resolve one full resonance dip and capture the WGM shifts, it is smaller than the resonators' free-spectral ranges (~65 GHz). The driving signal and the PMT outputs are fed to the data acquisition system. Figure 12 shows a sample laser voltage input, as well as the corresponding reference and sensing resonator spectra, over a time period covering two cycles of the scan. The location of the WGM dips is calculated for each positive and negative ramp. Therefore, the segment shown in the figure contains four individual measurements.

Two sets of measurements are carried out. In the first, the optical probe is located at a fixed position in the flow and the jet is switched on and off in quick successions for the same supply pressure. The objective of the experiment is to gauge the ability of the system to track large, sudden WGM shifts. In the second, velocity profiles are measured across the jet. For both experiments, the data is postprocessed to determine the WGM shifts and the corresponding velocity. Three different signal processing approaches are used to determine the WGM shifts: direct dip-detection, Cauchy–Lorentz function-fitting, and cross correlation. Direct dip-detection (where the minimum value and its spectral location is detected) has the shortest processing time. However, this is at the expense of accuracy, especially when the signal-to-noise levels are low. Cross correlation also possesses a small computational footprint, but requires additional preprocessing of the signal, especially with triangular-waveform scanning, rendering it more time consuming for larger data sets. Although Lorentzian fitting is computationally more taxing, it requires minimal preprocessing, offers the highest accuracy, and is capable of measuring shifts well below the full-width at half-max of the WGM dip. With the Lorentzian fitting, a WGM shift resolution of ~11.7 fm (16.5 MHz) is achieved, which translates into a velocity resolution of ~3.8 m/s in the current configuration.

The on/off measurements are performed at the centerline of the nozzle at $x/D = 0.787$. The jet is turned on and off by opening and closing the supply valve. The WGM shifts are calculated through the Lorentz function-fitting technique, and are then converted to velocity using Eq. (5) and the resonator calibration curves of Fig. 11. A typical result with several successive on/off states is shown in Fig. 13. Here, V represents the streamwise mean velocity [Eq. (4) and Fig. 8]. The total record length (integration time) for each data point in the figure
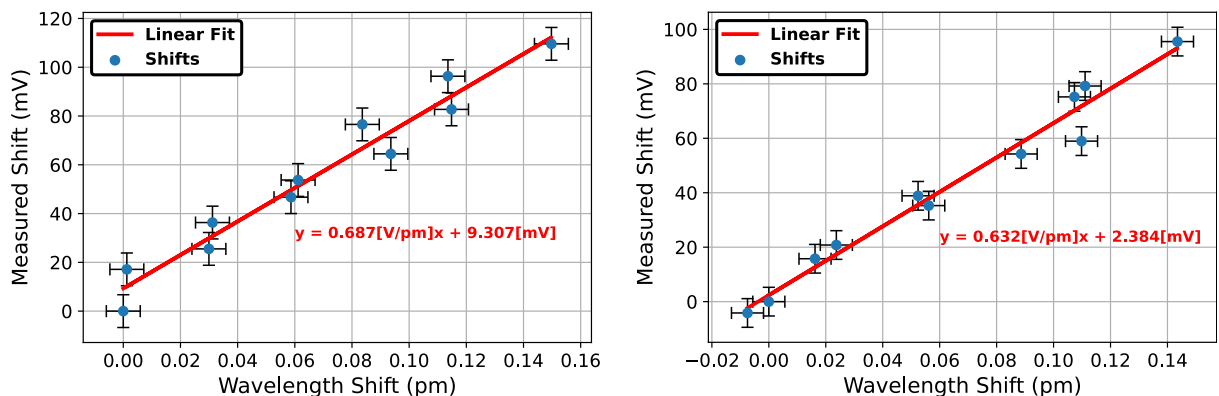

Fig. 11   Calibration for microresonators against the Fabry–Perot interferometer: Sensing resonator (left); reference resonator (right).
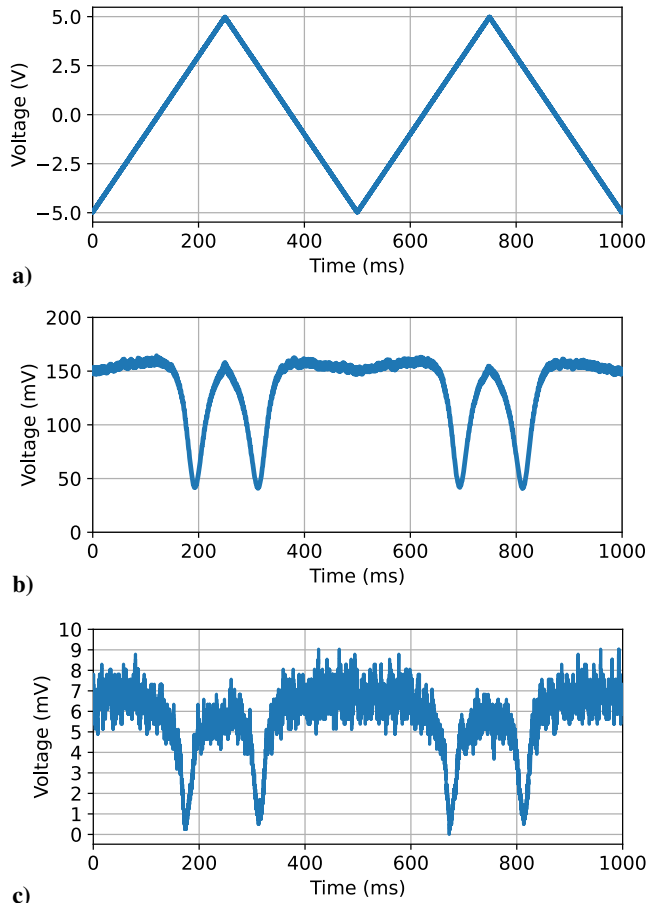
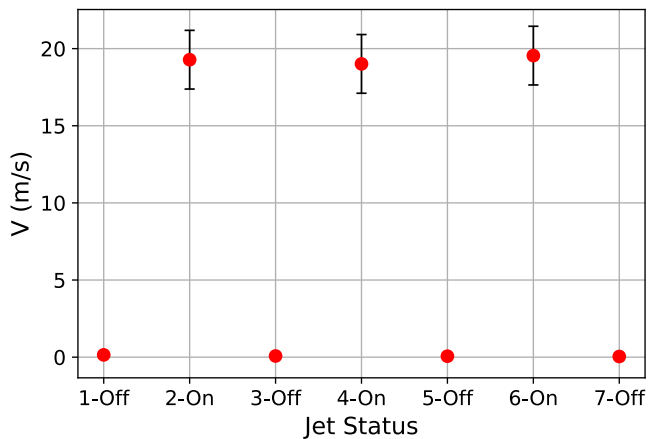**Fig. 12　Typical signal outputs during an experiment: a) laser driver, b) reference signal, and c) sensor signal.**
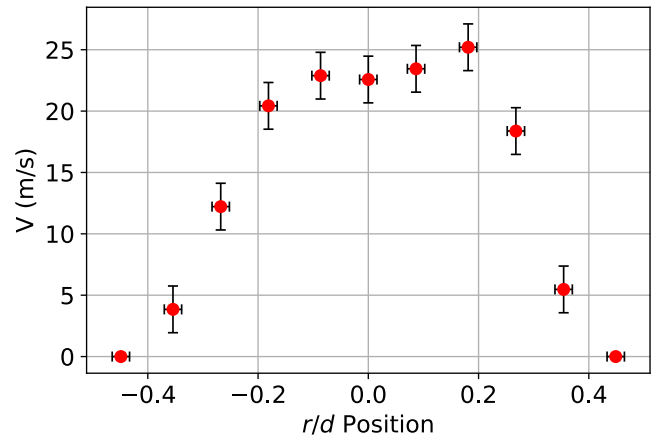

Fig. 13　On/off velocity measurements.

Fig. 14　Radial profile of mean streamwise velocity.

resolution, as described earlier. It is worth noting that the jet profile measurements are carried out using a small nozzle, which contributes to measurement error due to the uncertainty in the probe positioning.

V.　Conclusions

The proof-of-concept experiments demonstrate the viability of a WGM microresonator-based speed sensor. The jet results presented in Figs. 13 and 14 are encouraging, and the relatively large optical Q-factors of the resonators allow for high-velocity resolutions. The Lorentzian fitting of the resonances yields a shift resolution of ~11.7 fm (16.5 MHz), which translates to a velocity resolution of 3.8 m/s for the jet experiment setup. A full backscatter (monostatic) configuration would further improve this resolution considerably. The Q-factors of the ring resonators used in the current jet experiments are modest relative to typical WGM resonators, due to their small diameters. Employing larger resonators would increase these factors significantly. Another important consideration in the present sensor is the power of collected light reaching the detector. The coupling of free-space light into a single-mode optical fiber requires high precision in optical alignment. It is evident from the preliminary jet experiments that using standalone components for collecting optics and fiber ends results in substantial coupling losses. Use of integrated optics and grating-based couplers would significantly improve signal levels. Further, tuning the resonators (for example, via mechanical strain) instead of the input light to obtain the WGM spectra would allow using a fixed-wavelength laser, greatly simplifying the optical configuration. Because of its exceptional spectral filtering capabilities, the proposed microresonator-based sensor concept could possibly be extended to molecular scattering (Rayleigh–Brillouin) to measure other atmospheric quantities such as temperature, chemical species, and pollutants.

is 3.5 s, with the laser scanning at a rate of 2 Hz. Therefore, each data point is the average of 14 individual WGM spectra. The error bars represent the velocity resolution uncertainty of 3.8 m/s, based on the smallest detectable WGM shift discussed earlier.

Profiles of the mean streamwise velocity are obtained by mounting the jet nozzle on a high-precision three-dimensional-translation stage. Figure 14 shows the velocity profile at $x/D = 1.5$. Each data point represents the average of 48 individual laser scans, corresponding to a total integration time of 12 s per data point. Although some scatter in the data is present, the results clearly show the potential core region at the center (with the uniform velocity), and the surrounding shearing layer. The error bars along x direction represent the best precision of the translation stage. The error bars along y direction represent the velocity uncertainty related to the WGM measurement

References

[1] Theopold, F. A., and Bösenberg, J., "Differential Absorption Lidar Measurements of Atmospheric Temperature Profiles: Theory and Experiment," *Journal of Atmospheric and Oceanic Technology*, Vol. 10, No. 2, 1993, pp. 165–179.
https://doi.org/10.1175/1520-0426(1993)010<0165:DALMOA>2.0.CO;2

[2] Witschas, B., Lemmerz, C., and Reitebuch, O., "Daytime Measurements of Atmospheric Temperature Profiles (2–15 km) by Lidar Utilizing Rayleigh–Brillouin Scattering," *Optics Letters*, Vol. 39, No. 7, 2014,

pp. 1972–1975.
https://doi.org/10.1364/OL.39.001972

[3] Schiff, H., Mackay, G., and Bechara, J., "The Use of Tunable Diode Laser Absorption Spectroscopy for Atmospheric Measurements," *Research on Chemical Intermediates*, Vol. 20, No. 3, 1994, pp. 525–556.
https://doi.org/10.1163/156856794X00441

[4] Huey, L. G., "Measurement of Trace Atmospheric Species by Chemical Ionization Mass Spectrometry: Speciation of Reactive Nitrogen and Future Directions," *Mass Spectrometry Reviews*, Vol. 26, No. 2, 2007, pp. 166–184.
https://doi.org/10.1002/mas.20118

[5] Sprovieri, F., Pirrone, N., Ebinghaus, R., Kock, H., and Dommergue, A., "A Review of Worldwide Atmospheric Mercury Measurements," *Atmospheric Chemistry and Physics*, Vol. 10, No. 17, 2010, pp. 8245–8265.
https://doi.org/10.5194/acp-10-8245-2010

[6] Comerón, A., Muñoz-Porcar, C., Rocadenbosch, F., Rodrguez-Gómez, A., and Sicard, M., "Current Research in LIDAR Technology Used for the Remote Sensing of Atmospheric Aerosols," *Sensors*, Vol. 17, No. 6, 2017, p. 1450.
https://doi.org/10.3390/s17061450

[7] Charlson, R. J., Seinfeld, J. H., Nenes, A., Kulmala, M., Laaksonen, A., and Facchini, M. C., "Reshaping the Theory of Cloud Formation," *Science*, Vol. 292, No. 5524, 2001, pp. 2025–2026.
https://doi.org/10.1126/science.1060096

[8] Cziczo, D. J., Froyd, K. D., Hoose, C., Jensen, E. J., Diao, M., Zondlo, M. A., Smith, J. B., Twohy, C. H., and Murphy, D. M., "Clarifying the Dominant Sources and Mechanisms of Cirrus Cloud Formation," *Science*, Vol. 340, No. 6138, 2013, pp. 1320–1324.
https://doi.org/10.1126/science.1234145

[9] George, J. J., *Weather Forecasting for Aeronautics*, Academic Press, New York, 2014.

[10] Shimada, T., and Kurokawa, K., "Insolation Forecasting Using Weather Forecast with Weather Change Patterns," *IEEJ Transactions on Power and Energy*, Vol. 127, No. 11, 2007, pp. 1219–1225.
https://doi.org/10.1541/ieejpes.127.1219

[11] Chahine, M. T., Pagano, T. S., Aumann, H. H., Atlas, R., Barnet, C., Blaisdell, J., Chen, L., Divakarla, M., Fetzer, E. J., Goldberg, M., Gautier, C., Granger, S., Hannon, S., Irion, F. W., Kakar, R., Kalnay, E., Lambrigsten, B. H., Lee, S.-Y., Le Marshall, J., Mcmillan, W. W., Mcmillin, L., Olsen, E. T., Revercomb, H., Rosenkranz, P., Smith, W. L., Staelin, D., Strow, L. L., Susskind, J., Tobin, D., Wolf, W., and Zhou, L., "AIRS: Improving Weather Forecasting and Providing New Data on Greenhouse Gases," *Bulletin of the American Meteorological Society*, Vol. 87, No. 7, 2006, pp. 911–926.
https://doi.org/10.1175/BAMS-87-7-911

[12] Peral, E., Im, E., Wye, L., Lee, S., Tanelli, S., Rahmat-Samii, Y., Horst, S., Hoffman, J., Yun, S.-H., Imken, T., and Hawkins, D., "Radar Technologies for Earth Remote Sensing from CubeSat Platforms," *Proceedings of the IEEE*, Vol. 106, No. 3, 2018, pp. 404–418.
https://doi.org/10.1109/jproc.2018.2793179

[13] Gasiewski, A. J., Sanders, B. T., and Gallaher, D., "CubeSat Based Sensors for Global Weather Forecasting," *2013 US National Committee of URSI National Radio Science Meeting (USNC-URSI NRSM)*, Inst. of Electrical and Electronics Engineers, New York, 2013, pp. 1–1.
https://doi.org/10.1109/usnc-ursi-nrsm.2013.6525008

[14] Blackwell, W. J., "The MicroMAS and MiRaTA CubeSat Atmospheric Profiling Missions," *2015 IEEE MTT-S International Microwave Symposium*, Inst. of Electrical and Electronics Engineers, New York, 2015, pp. 1–3.
https://doi.org/10.1109/mwsym.2015.7166742

[15] Blackwell, W., "New CubeSat Observing Capabilities for Microwave Atmospheric Sensing," *Sensors, Systems, and Next-Generation Satellites XXII*, Vol. 10785, International Soc. for Optics and Photonics, Bellingham, WA, 2018, Paper 1078504.
https://doi.org/10.1117/12.2324319

[16] Kays, M., and Olsen, R., "Improved Technique for Deriving Wind Profiles from Rocketsonde Parachutes," *Journal of Geophysical Research*, Vol. 72, No. 16, 1967, pp. 4035–4040.
https://doi.org/10.1029/JZ072i016p04035

[17] Jenkins, K. R., "Empirical Comparisons of Meteorological Rocket Wind Sensors," *Journal of Applied Meteorology (1962-1982)*, Vol. 1, No. 2, 1962, pp. 196–202.
https://doi.org/10.1175/1520-0450(1962)001<0196:ecomrw>2.0.co;2

[18] Esposito, F., Montmessin, F., Debei, S., Colombatti, G., Harri, A.-M., Pommereau, J.-P., Wilson, C., Aboudan, A., Molfese, C., Zaccariotto, M., and Mugnuolo, R., "The DREAMS Payload On-Board the Entry and Descent Demonstrator Module of the ExoMars Mission," *EGU General Assembly Conference Abstracts*, European Geosciences Union (EGU), Munich, Germany, 2012, p. 9722.

[19] Gómez-Elvira, J., Armiens, C., Castañer, L., Domnguez, M., Genzer, M., Gómez, F., Haberle, R., Harri, A.-M., Jiménez, V., Kahanpää, H., Kowalski, L., Lepinette, A., Martín, J., Martínez-Frías, J., McEwan, I., Mora, L., Moreno, J., Navarro, S., de Pablo, M. A., Peinado, V., Peña, A., Polkko, J., Ramos, M., Renno, N. O., Ricart, J., Richardson, M., Rodriguez-Manfredi, J., Romeral, J., Sebastián, E., Serrano, J., de la Torre Juárez, M., Torrero, F., Urquí, R., Vázquez, L., Velasco, T., Verdasca, J., Zorzano, M. P., and Martín-Torres, J., "REMS: The Environmental Sensor Suite for the Mars Science Laboratory Rover," *Space Science Reviews*, Vol. 170, No. 1, 2012, pp. 583–640.
https://doi.org/10.1007/s11214-012-9921-1

[20] Huffaker, R. M., "Laser Doppler Detection Systems for Gas Velocity Measurement," *Applied Optics*, Vol. 9, No. 5, 1970, pp. 1026–1039.
https://doi.org/10.1364/AO.9.001026

[21] Hughes, A., and Pike, E., "Remote Measurement of Wind Speed by Laser Doppler Systems," *Applied Optics*, Vol. 12, No. 3, 1973, pp. 597–601.
https://doi.org/10.1364/AO.12.000597

[22] Truax, B. E., Demarest, F. C., and Sommargren, G. E., "Laser Doppler Velocimeter for Velocity and Length Measurements of Moving Surfaces," *Applied Optics*, Vol. 23, No. 1, 1984, pp. 67–73.
https://doi.org/10.1364/AO.23.000067

[23] Vaughan, J., and Forrester, P., "Laser Doppler Velocimetry Applied to the Measurement of Local and Global Wind," *Wind Engineering*, Vol. 13, No. 1, 1989, pp. 1–15.

[24] Cao, X., Liu, J., Jiang, N., and Chen, Q., "Particle Image Velocimetry Measurement of Indoor Airflow Field: A Review of the Technologies and Applications," *Energy and Buildings*, Vol. 69, Feb. 2014, pp. 367–380.
https://doi.org/10.1016/j.enbuild.2013.11.012

[25] Koschatzky, V., Moore, P., Westerweel, J., Scarano, F., and Boersma, B., "High Speed PIV Applied to Aerodynamic Noise Investigation," *Experiments in Fluids*, Vol. 50, No. 4, 2011, pp. 863–876.
https://doi.org/10.1007/s00348-010-0935-8

[26] Kavaya, M. J., Henderson, S. W., Magee, J. R., Hale, C. P., and Huffaker, R. M., "Remote Wind Profiling with a Solid-State Nd: YAG Coherent Lidar System," *Optics Letters*, Vol. 14, No. 15, 1989, pp. 776–778.
https://doi.org/10.1364/OL.14.000776

[27] Wächter, M., Rettenmeier, A., Kühn, M., and Peinke, J., "Wind Velocity Measurements Using a Pulsed Lidar System: First Results," *14th International Symposium for the Advancement of Boundary Layer Remote Sensing*, Vol. 1, IOP Publishing, Bristol, U.K., 2008, Paper 012066.
https://doi.org/10.1088/1755-1315/1/1/012066

[28] Iwai, H., Ishii, S., Oda, R., Mizutani, K., Sekizawa, S., and Murayama, Y., "Performance and Technique of Coherent 2-μm Differential Absorption and Wind Lidar for Wind Measurement," *Journal of Atmospheric and Oceanic Technology*, Vol. 30, No. 3, 2013, pp. 429–449.
https://doi.org/10.1175/JTECH-D-12-00111.1

[29] Irgang, T. D., Hays, P. B., and Skinner, W. R., "Two-Channel Direct-Detection Doppler Lidar Employing a Charge-Coupled Device as a Detector," *Applied Optics*, Vol. 41, No. 6, 2002, pp. 1145–1155.
https://doi.org/10.1364/AO.41.001145

[30] Seasholtz, R. G., "2D Velocity and Temperature Measurements in High Speed Flows Based on Spectrally Resolved Rayleigh Scattering," *New Trends in Instrumentation for Hypersonic Research*, Springer, Dordrecht, The Netherlands, 1993, pp. 399–408.
https://doi.org/10.1007/978-94-011-1828-6_37

[31] Bivolaru, D., Danehy, P. M., and Lee, J. W., "Intracavity Rayleigh-Mie Scattering for Multipoint, Two-Component Velocity Measurement," *Optics Letters*, Vol. 31, No. 11, 2006, pp. 1645–1647.
https://doi.org/10.1364/OL.31.001645

[32] Zheng, J., *Optical Frequency-Modulated Continuous-Wave (FMCW) Interferometry*, Vol. 107, Springer, New York, 2005, pp. 7–44.

[33] da Silva, J., Salameh, E., Ötügen, M. V., and Fourguette, D., "Sensors Based on Evanescent Field Perturbation of Microresonators," *Applied Optics*, Vol. 60, No. 5, 2021, pp. 1434–1439.
https://doi.org/10.1364/AO.417187

[34] Ioppolo, T., Kozhevnikov, M., Stepaniuk, V., Ötügen, M. V., and Sheverev, V., "Micro-Optical Force Sensor Concept Based on Whispering Gallery Mode Resonators," *Applied Optics*, Vol. 47, No. 16, 2008, pp. 3009–3014.
https://doi.org/10.1364/ao.47.003009

[35] Ioppolo, T., and Ötügen, M. V., "Pressure Tuning of Whispering Gallery Mode Resonators," *Journal of the Optical Society of America B*, Vol. 24,

No. 10, 2007, pp. 2721–2726.
https://doi.org/10.1364/JOSAB.24.002721

[36] Manzo, M., Ioppolo, T., Ayaz, U., LaPenna, V., and Ötügen, M., "A Photonic Wall Pressure Sensor for Fluid Mechanics Applications," *Review of Scientific Instruments*, Vol. 83, No. 10, 2012, Paper 105003.
https://doi.org/10.1063/1.4757569

[37] Ayaz, U., Ioppolo, T., and Ötügen, M., "Wall Shear Stress Sensor Based on the Optical Resonances of Dielectric Microspheres," *Measurement Science and Technology*, Vol. 22, No. 7, 2011, Paper 075203.
https://doi.org/10.1088/0957-0233/22/7/075203

[38] Ioppolo, T., Ayaz, U., and Ötügen, M. V., "Tuning of Whispering Gallery Modes of Spherical Resonators Using an External Electric Field," *Optics Express*, Vol. 17, No. 19, 2009, pp. 16465–16479.
https://doi.org/10.1364/OE.17.016465

[39] Ioppolo, T., Ötügen, M., and Marcis, K., "Magnetic Field-Induced Excitation and Optical Detection of Mechanical Modes of Microspheres," *Journal of Applied Physics*, Vol. 107, No. 12, 2010, Paper 123115.
https://doi.org/10.1063/1.3452363

[40] Ötügen, M. V., Su, W.-J., and Papadopoulos, G., "A New Laser-Based Method for Strain Rate and Vorticity Measurements," *Measurement Science and Technology*, Vol. 9, No. 2, 1998, p. 267.
https://doi.org/10.1088/0957-0233/9/2/015

[41] Wise, B. J., Eghbalifarkoosh, V., Otugen, V., and Fourguette, D., "A Microresonator Based Laser Velocity Sensor," *2018 AIAA Aerospace Sciences Meeting*, AIAA Paper 2018-1770, 2018.
https://doi.org/10.2514/6.2018-1770

[42] Wise, B. J. A., "A Microresonator-Based Laser Doppler Velocity Sensor For Interplanetary Atmospheric Re-Entry," Master's Thesis, Southern Methodist Univ., Dallas, TX, 2018.

[43] Zaoui, W. S., Kunze, A., Vogel, W., Berroth, M., Butschke, J., Letzkus, F., and Burghartz, J., "Bridging the Gap Between Optical Fibers and Silicon Photonic Integrated Circuits," *Optics Express*, Vol. 22, No. 2, 2014, pp. 1277–1286.
https://doi.org/10.1364/OE.22.001277

I. Gursul
Associate Editor